Optimization of STEM-HAADF electron tomography reconstructions by parameter selection in compressed sensing Total Variation Minimization-based algorithms

Juan M. Muñoz-Ocaña[1], Ainouna Bouziane[2], Farzeen Sakina[3], Richard T. Baker[3], Ana B. Hungría[2], Jose J. Calvino[2], Antonio M. Rodríguez-Chía[1], Miguel López-Haro[2]

[1] Departamento de Estadística e Investigación Operativa, Facultad de Ciencias, Universidad de Cádiz, Campus Puerto Real, 11510-Puerto Real, Cádiz.
[2] Departamento de Ciencia de los Materiales e Ingeniería Metalúrgica y Química Inorgánica, Facultad de Ciencias, Universidad de Cádiz, Campus Puerto Real, 11510-Puerto Real, Cádiz.
[3] EaStChem, School of Chemistry, University of St Andrews, St Andrews, Fife, KY16 9ST, United Kingdom

Keywords: 3D characterization, STEM-HAADF electron tomography, compressed-sensing, parameters selection, mesoporous materials

A novel procedure to optimize the 3D morphological characterization of nanomaterials by means of High Angle Annular Dark Field Scanning-Transmission Electron Tomography (HAADF-STEM-ET) is reported and fruitfully applied to the analysis of a metal and halogen-free ordered mesoporous carbon material. The new method is based on a selection of the two parameters (μ and β) which are key in the reconstruction of tomographic series by means of Total Variation Minimization (TVM). The parameter-selected TVM reconstructions obtained using this approach clearly reveal the porous structure of the carbon-based material as consisting of a network of parallel, straight channels of ~ 6 nm diameter and ordered in a honeycomb-type arrangement. Such an unusual structure could not be retrieved from a TVM3D reconstruction using default reconstruction values. Moreover, segmentation and further quantification of the optimized 3D tomographic reconstruction provided values for different textural parameters, such as pore size distribution and specific pore volume, that matched very closely those determined by macroscopic physisorption techniques. The approach developed can be extended to other reconstruction models in which the final result is influenced by parameter choice.

1. Introduction

3D morphological analysis of nanostructured materials by means of Electron Tomography (ET) is currently a well-stablished approach which provides meaningful information out of the reach of conventional 2D TEM/STEM analysis.[1]

In the ET experiment, a series of 2D images are acquired at different tilts of the sample under analysis with respect to the incoming electron beam, usually around only one axis. Back-projection of the information contained in each of these images by different mathematical procedures (algorithms) allows the retrieval of the 3D morphology of the object which produced the set of recorded 2D projections. The size of the tilt range and the total number of projections (tilt increment) influence the quality of the reconstruction in terms of resolution and contribution of image artifacts, like elongation of the object in the direction perpendicular to the tilting axis (the so-called missing wedge effect).[2] Therefore, maximizing, within the achievable experimental limits, these two parameters were initially considered as the essential ingredient of the recipe to obtain optimum tomographic reconstructions.

Nevertheless, the development of analytical STEM tomography[3] as well as the need to minimize, especially in the case of beam sensitive materials, the influence of beam damage, have contributed to focus most of the research in the field on the development of methodologies. The main goal of these methodologies is to keep or even to improve the quality of the reconstructed volumes in experiments in which the amount of available information becomes, even severely, reduced.

Different strategies have been proposed to reach this goal, such as limiting the tilt range, decreasing the number of projections or decreasing the number of sampled image points in each projection, e.g. by scanning only a random selection of image points.[4]

To compensate the loss of information involved by any of these strategies, an enhancement of the reconstruction step of the tomographic experiment is required. Methods based on Compressed Sensing (CS), which exploit the minimization of the Total Variation (l_1-norm or l_2 norm) of the intensity gradient of the whole set of images in the tilt series, have proven to be quite efficient at this respect.[5] Therefore, though the more conventional reconstruction approaches, such as SIRT (Simultaneous Iterative Reconstruction Technique), are still widely employed, the use of CS-TVM is continuously increasing as an alternative to tackle tomography data obtained under more restrictive experimental conditions.[6]

Several methods have been reported to implement CS-TVM,[5a, 7] but that proposed by Li et al. known as TVAL3,[8] is the widely used in STEM tomography, since it allows the solution of large scale instances, as is required when working with projected images containing a large number of pixels.[5b] The practical implementation of TVAL3 involves the use of two a priori, user-fixed, parameters, μ and β, which provide, respectively, a balance between the level of image detail and the match between the experimental and reconstructed sinograms (see expression (2) for further details). The choice of the values of these parameters for a particular reconstruction is made by visual judgment of the tilt series image features, including the noise level and, particularly, based on previous experience in the analysis of similar problems. In any case, such parameters are fixed arbitrarily, which does not guarantee a good approximation to the most accurate solution possible within that range.

Therefore, it seems clear that the correct choice of the CS-TVM algorithm parameters, within a set of reasonable variation range, by automated, user-independent procedures would not only allow improved reconstructions to be obtained but also guarantee that such reconstructions represent, with a large degree of certainty, the most accurate solution possible within that range. Such accuracy should be estimated by an equation that reasonably measures the deviation between the experimental and reconstructed sinograms.

In this paper we address the key question of the correct choice of the parameter selection method in the case of CS-TVM reconstructions. A methodology is proposed and tested for the reconstruction of STEM-HAADF tilt series to allow the 3D morphological analysis of a material with potential application as a nanocatalyst support, namely an ordered mesoporous carbon material. This material was prepared by a synthetic route which avoids the retention of undesirable metallic or halogen residues - which otherwise may act as catalyst poisons - within the carbon structure.[6a, 9]

Nanocatalysis stands out as one of the fields which have greatly profited from the 3D characterization capabilities of Electron Tomography, not only in the STEM-HAADF mode but also, for some particular types of materials, in the Bright Field Transmission Electron Microcopy mode (TEM-BF).[10] This is in fact the case for porous materials, whose adsorptive and transport properties are intimately related to specific structural features of their pore system, such as pore width and length distributions, tortuosity or internal and external connectivity. Electron tomography has demonstrated itself to be a unique technique to reveal, in a fully quantitative way, all of these aspects.[11]

The quantification of any property from a 3D tomographic reconstruction requires the identification (partitioning) of the whole volume into separate objects corresponding to its different physical components. Thus, in the analysis of the pore structure of any material the subset of volume elements (voxels) of the reconstruction corresponding to vacuum (void) must be identified. This step of the quantitative analysis of a 3D reconstruction is known as segmentation and it usually involves the use of some intensity thresholding method to separate objects from background or to distinguish between different type of objects. In general, segmentation is a critical step in the quantitative analysis of 3D reconstructions and, particularly, in the analysis of the morphological properties of porous materials.

In the specific case of porous materials in the form of powders, different reports have pointed out the benefits, in terms of segmentation fidelity, of using reconstruction algorithms based on

Discrete Algebraic Reconstruction Techniques (DART), which try to minimize the difference between the experimental sinogram and the reconstructed sinogram taking into account that the image can only contain a discrete number of gray levels. Their lower sensitivity to the influence of reconstruction-induced artifacts, like elongation due to the so-called missing wedge effect, and their intrinsic simplicity, since thresholding is already part of the reconstruction process, are highlighted as the most important benefits.[11a]

Recently, Lopez-Haro et al.[12] have demonstrated that the combination of image-denoising by Undecimated Wavelet Transforms[13] with advanced segmentation procedures and CS-TVM reconstruction with default recommended values, allow a fully automated quantification of tomographic experiments recorded on supported metal type nanocatalyst samples. Moreover, these authors have shown that the quantitative parameters obtained after applying this combined approach to a batch of tilt series recorded on a Au/CeO_2 catalyst matched very closely those determined by macroscopic characterization techniques.

Nevertheless, since the minimization of the l_1-norm and l_2-norm of the image gradient performed during CS-TVM leads to reconstructed volumes made up of regions of locally constant intensity separated by sharp interfaces, it is not clear if this approach is appropriate for the particular case of porous materials, in which the interfaces between pores and material may appear in the images as areas of more smoothly varying contrasts.

Now, in this paper, it is demonstrated that the approach described in[12] can also be fruitfully applied to materials comprising a system of nanopores but, in this particular case, on the basis of parameter-optimized CS-TVM reconstructions. Moreover, the paper illustrates how CS-TVM reconstructions with default recommended values fail to reveal the pore system of the ordered mesoporous carbon sample studied whereas the optimized reconstructions allow the clear identification and quantification, after smart segmentation, of properties including the specific pore size distribution and specific pore volume. Importantly, the values of these parameters estimated from a collection of tomographic experiments recorded in a fully

automated batch mode are, once more, in close agreement with measurements performed by macroscopic physisorption techniques, which clearly demonstrates the reliability of the proposed method.

2. Results

The two major goals of the present work are, first, to develop a feasible method that, within a reasonable execution time, would allow, in a reliable way, improved CS-TVM reconstructions to be attained by choice of the optimum values for the two parameters involved in this algorithm. Secondly, the appropriateness of the CS-TVM approach to the 3D morphological analysis of porous materials is considered, particularly in connection with the use of default recommended parameters versus parameter-optimized CS-TVM reconstructions.

2.1. Development of a parameter optimization method for CS-TVM reconstructions

The mathematical model involved in a CS-TVM reconstruction can be written as follows:

$$\min_x \sum_i ||D_i x||_2 + \frac{\mu}{2}||Ax - b||_2^2 - \sigma(Ax - b) \qquad (1)$$

where $x \in \mathbb{R}^{n^2}$ is the reconstructed ($n \times n$) image, i.e. the solution of the minimization problem; $b \in \mathbb{R}^{np \cdot n}$ is the sinogram of x, with np the number of projections in the tilt series; A is the projection matrix and Di calculates the gradient of x at pixel i according to

$$(x_i - x_{i+1}, x_i - x_{n+i})$$

Then, variables y_i are added to the problem (1) as a set of constraints $D_i x = y_i$ to obtain a differentiable objective function from x, i.e.,

$$\min_x \sum_i ||y_i||_2 + \frac{\mu}{2}||Ax - b||_2^2 - \sigma(Ax - b)$$

$$s.t. \quad D_i x = y_i, \quad i = 1, \dots, n^2$$

Constraints $D_i\, x = y_i$ are relaxed by the augmented Lagrangean relaxation approach:

$$\min_{x,y} \sum_i (||y_i||_2 + \frac{\beta}{2}||D_i x - y_i||_2^2 - \gamma_i(D_i x - y_i)) + \frac{\mu}{2}||Ax - b||_2^2 - \sigma(Ax - b) \qquad (2)$$

Finally, γ and σ are the Lagrange multipliers which are updated after each iteration of the minimization process, usually through a subgradient method, as follows:

$$\sigma_k = \sigma_{k-1} - \mu(Ax - b) \qquad (3)$$

$$\gamma_{i,k} = \gamma_{i,k-1} - \beta(D_i x - y_i) \qquad (4)$$

where *k* stands for the iteration number in the subgradient method. See [8] for further details.

As already mentioned in the introduction, μ and β are penalty parameters which have to be fixed for a particular CS-TVM reconstruction.

From the expression of the objective function (Equation 1) it is clear that μ penalizes the difference between the initial data (i.e. the projected images recorded in the tilt series), *b,* and the reconstructed sinogram *Ax*. Consequently, high μ values lead to increased image detail. In general, the higher the value of this parameter, the closer the reconstruction is to that obtained by SIRT.

Since β is the weighting factor of the term containing the contribution of the squared l_2-norm of the gradient ($D_i x$), it controls the smoothing level of the solution. In other words, high values of β remove image details and increase the presence of constant intensity regions (patches or stripes) in the reconstructed volume.

Given the counterbalanced role of these two parameters, an appropriate selection should allow a solution to be obtained which, while still showing a low total variation, depicts the contrast details of the experimental sinogram.

Figure S1 illustrates in a pictorial way the effect of each of these two parameters on the reconstruction of a 128 x 128 version of the well-known Shepp-Logan 2D phantom (128 x 128

image). In these calculations, which considered 2º tilt increments from -70º to 70º, one of the parameters is kept fixed and the second changed over a very wide range, from 2^1 to 2^{20}. To approach more realistic experimental conditions, the initial phantom was corrupted with Poisson (λ=100) and Gaussian (σ=2) noise, which provided a signal to noise ratio (S/N) of roughly 15.2 dB, close to that found in our STEM HAADF images, recorded in the conditions mentioned in the experimental section.

Note from **Figure S1** that, the higher the value of μ, the greater the details in the resulting image. In fact, high μ values do not reduce noise from the image, but low μ values remove too many details. In the two extreme cases, the small ovals present in the phantom are lost in the reconstruction. Note also how increasing the value of μ clearly reduces the deformation (elongation) of the large oval, an effect which is particularly evident at the top and bottom apexes of this oval as well as in the variation of the intensity along the outer rim. This indicates an effective reduction of the missing wedge effect at increasing values of μ.

In contrast to that previously described for the μ parameter, low β values result in reconstructions with finer details, whereas high β values lead to blurred images. Concerning the influence of the missing wedge, a trend contrary to that occurring with μ is also observed, since the lowest β values more effectively reduce this effect.

On the basis of these results one could expect that very detailed images could be recovered using a high μ and low β combination. However, this is not the case because such a parameter selection does not remove efficiently the noise content of the reconstruction. However, a high image quality is expected by carefully selecting (balancing) these two parameters, the final position of the balance being linked to the actual noise content of the tilt series. Thus, a compromise between both parameters must be found to recover a high-quality reconstruction.

Figure S2 shows analogous result but using a phantom which contains structural features closer to those expected in mesoporous systems, particularly in ordered mesoporous materials, such

as those considered in the experimental ET study presented in a later section. Note how also in this case a compromise between both parameters is necessary to reach an optimum reconstruction.

A brute force search for such a compromise combination is a tedious and time-consuming process since a large set of complete reconstructions should be performed in order to screen a wide enough parameter space. Let us recall in this respect that currently common execution times for a single CS-TVM reconstruction of a tilt series involving a few tens (e.g. 70) of 1k×1k images may take a few hours. Therefore, a procedure which allows this search to be speeded up in an efficient and automated way is required. To reach this goal we have considered as a starting point the fact that, in the case of 2D images, such as those shown in **Figures S1** and **S2**, the computational time is greatly reduced even when large images (e.g. 1k×1k) are involved. In the next section such a procedure is described in detail using TVAL3. This approach would also be valid for other parametrized reconstruction algorithms.

2.1.1. A procedure for the automated choice of CS-TVM reconstruction parameters

We will consider a tilt series comprising n_p images of $m \times m$ pixels in size, that is a $m \times m \times n_p$ sinogram as the initial dataset. In a first step, this sinogram is split into m slices of $m \times n_p$ pixels and s slices are selected from these. These s slices are chosen to be equally spaced from each other to select as much information as possible from the whole sinogram. Once these s slices are chosen, TVAL3 is applied to each one with a large set of parameter choices ($\mu=2^1, 2^2,\ldots, 2^p$) and ($\beta=2^1, 2^2,\ldots, 2^q$). This gives rise to a total of $p \cdot q$ CS-TVM reconstructions of 2D images. Though only s slices are chosen in order to keep the total computation time within reasonable limits, this parameter can be freely changed, depending on the power of the available computation facilities. Thus, TVAL3 is applied $p \cdot q$ times to recover each single slice with all possible parameter combinations. The application of this procedure to find the best (μ, β) parameter combination using TVM3D, instead of TVM, leads to quite close, hardly

distinguishable, results **(Figure S3)**. However, the computation time required for the optimization step using TVM3D becomes one order of magnitude higher, which renders it useless.

After recovering each slice with the different combination of parameters, their sinograms, $Ax=b$, are calculated and compared with the experimental sinogram. For such comparison, the difference (ρ) between the initial and reconstructed sinogram is calculated as follows:

$$\rho = \frac{\left\| \frac{B}{\max(B)} - \frac{b}{\max(b)} \right\|_2}{\left\| \frac{b}{\max(b)} \right\|_2} \quad (5)$$

where b is the initial sinogram, B is the reconstructed sinogram, and $\max(b)$ and $\max(B)$ are the maximum values from both sinograms. This normalized difference, ρ, can be taken as the normalized error of the reconstruction. Observe that in the expression above $\min(b)$ and $\min(B)$ values do not appear, since the experimental STEM HAADF images were preprocessed to set the background to zero, to guarantee a 0 minimum value for b. As previously reported, [5a] this is an important step to improve the quality of the reconstructions. Additionally, the A matrix will contain at least one zero-valued row, which ensures a 0 minimum value for B.

Figure S4 shows the normalized error values for the reconstruction of the 2D Shepp-Logan phantom using μ and β combinations in a wider range than that considered in Figure 1. In this case, it is observed that β has a large influence on the image quality at low μ values. However, large μ values lead to high quality reconstructions regardless of the value of β.

The evolution of the normalized error values with μ for fixed β values is illustrated in **Figure 1** where $\beta = (2^1, \dots, 2^9)$ and μ takes values from 2^6 to 2^{30} for each β value. Note that after a large drop of ρ with increasing μ, fluctuations are observed with local peaks of large ρ values, which evidences the difficulties of reaching a good solution by a default recommended values of (μ,β).

For each slice, a $p \times q$ error matrix can be built gathering the error values calculated for each specific (μ, β) pair, such as that shown in **Table S1**. As observed, the parameter space is screened over quite a wide area, in this particular case in the 2^1-2^{20} and 2^1-2^{12} range for μ and β, respectively. The minimum value in this matrix, highlighted in red, corresponds to the combination of parameters which leads to the best reconstruction among the studied combination of parameters for that particular slice.

After repeating this procedure *s* times (once for each of the selected slices), a cumulative error matrix is calculated by simple addition of the *s* individual error matrices. To avoid the bias which could be introduced by a single error value with a large deviation within the 12-member set, the highest error is removed for each (μ, β) combination. Therefore, the cumulative error of each parameter combination is obtained by adding $s - 1$ values.

The μ and β combination corresponding to the minimum in the cumulative error matrix is the one chosen to finally reconstruct the whole set of images in the tilt series (not just the *s* subset) using TVM3D. This last, volumetric, implementation of the TVM algorithm allows the influence of striping effects usually observed with TVM2D to be mitigated.[12, 14] The different steps involved in the proposed methodology are summarized in the flow chart of **Figure S5**.

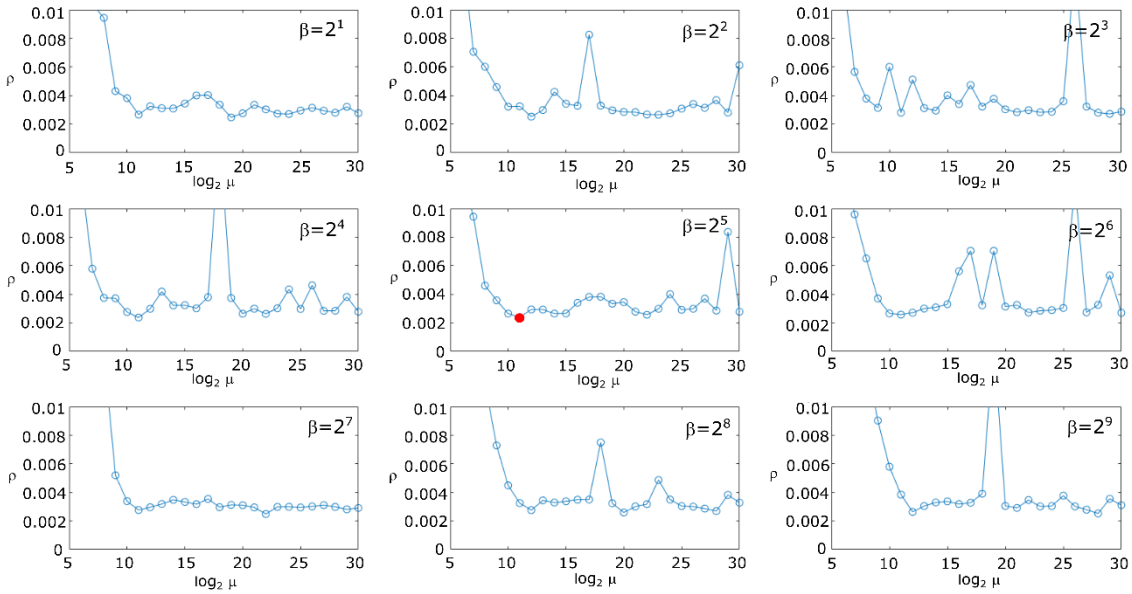

Figure 1.- Normalized error (ρ) in the TVM2D reconstruction of the Shepp-Logan phantom for different (μ, β) combinations. ρ vs $\log_2(\mu)$ plots for different fixed β values are shown. The minimum ρ value ($2.4 \cdot 10^{-3}$) has been marked with a red line.

Searching for (μ,β) pairs which allow minimising the deviation between experiment and reconstruction may lead to a result in which a significant noise level is still retained, despite TVM dampens it to some extent. It has to be taken into account that the algorithm searches the appropriate (μ,β) combination by comparing reconstructed and original sinograms. So, in case that the initial data set is not denoised, the output will depict a good noise reconstruction. Therefore, denoising the initial sinogram is a crucial step to reach the best output using the proposed parameter selection method. To illustrate this point, **Figure S7** shows the difference between a segmentation from a denoised sinogram and from a noisy one. The original phantom consisted of an ordered arrangement of pores with an area equivalent to 20 pixels. Note how the reconstruction obtained from the noisy sinogram leads to a segmentation in which the pore structure is hardly recognizable, despite the fact that the (μ,β) pair has been selected. When the sinogram is first denoised, the optimization process leads to a different (μ,β) pair and, in clear contrast, the segmentation of the image reconstructed using this new pair reflects quite closely the porous structure. A quantitative comparison between both results can be made on the basis of the pore size histograms determined from the segmented reconstructions. Thus, the histogram of the image reconstructed from the denoised sinogram shows a narrow distribution peaking at a pore size of 19 px^2, a value which only very slightly underestimates the pore size in the original phantom, 20 px^2. The histogram of the segmentation obtained from the noisy sinogram shows a very wide pore size distribution, with a large contribution from very small pores, which are not present in the original model, due to the presence of noise.

On the other hand, the application of this procedure to find the best (μ, β) parameter combination using TVM3D, instead of TVM, has been also carried out. Note how the parameters obtained lead to quite close, hardly distinguishable results (**Figure S10**). However, the computation time required for the optimization step using TVM3D becomes one order of magnitude higher, which renders it useless.

2.2. Testing the automatic parameter-selection method in the reconstruction of mesoporous catalysts.

In this section, the potential to improve experimental CS-TVM reconstructions of the methodology developed is evaluated and the question of whether the TVM approach is adequate to address the morphological characterization of mesoporous materials is posed, since such materials may initially appear not to fully comply with the assumptions underlying this regularization scheme.

Figure 2 shows different perspective views of the 3D-rendered volumes of tomographic CS-TVM reconstructions of an ordered mesoporous carbon sample. In particular, **Figure 2(b)** corresponds to a reconstruction using default recommended values for μ and β parameters, whereas **Figure 2(a)** depicts the result obtained after applying the automated selection method developed in this work, after screening a large range of the parameter space. Prior to reconstruction, the images in the tilt series were, in both cases, denoised by means of Undecimated Wavelet Transforms (UWT).

It is evident that there is a large improvement in the recovery of the morphological details after applying our procedure for choosing the parameters for the reconstruction. In fact, the honeycomb-like distribution of straight pores is appreciated practically across the whole particle in the different views in **Figure 2(a),** whereas it is hardly observed in any of the three included in **Figure 2(b).** A set of reconstructions obtained using a large parameter range are

shown in **Figure S8.** It is clear once more that a compromise between both parameters is necessary to obtain a high quality reconstruction.

The improvement associated with the selection method is also clearly observed in the comparison of orthoslices across the reconstructed volume, as shown in **Figure 3**. Note that in the orthoslices through the reconstruction obtained by the default recommended values, Figure 4(b), only a very small number of pores show a large contrast with respect to the carbon matrix. Most of them appear as if blocked with material and in fact, during the segmentation of these orthoslices, as shown later, most pores are not detected. On the contrary, in the orthoslices of the reconstruction obtained after parameter-selection, Figure 4(a), a huge number of pores showing a large contrast with respect to the carbon matrix is observed.

To compute the pore size distribution, the reconstructed volume obtained by parameter selection was first segmented by using a semiautomatic procedure based on the Multi-Otsu algorithm recently developed in our laboratory (Step b in Figure S9). [12] To separate the pores from the matrix, the already segmented volume was filled (step c in Figure S9). Then, this new volume was used as template. Arithmetic subtraction of the binarized carbon matrix volume from the filled template (step d in Figure S9) leads to an image in which the pores are fruitfully separated from the matrix. Finally, an open morphological operation was performed to remove some artefacts. **Figure 4** displays the blue areas in the two segmentations correspond to the pores detected after segmentation.

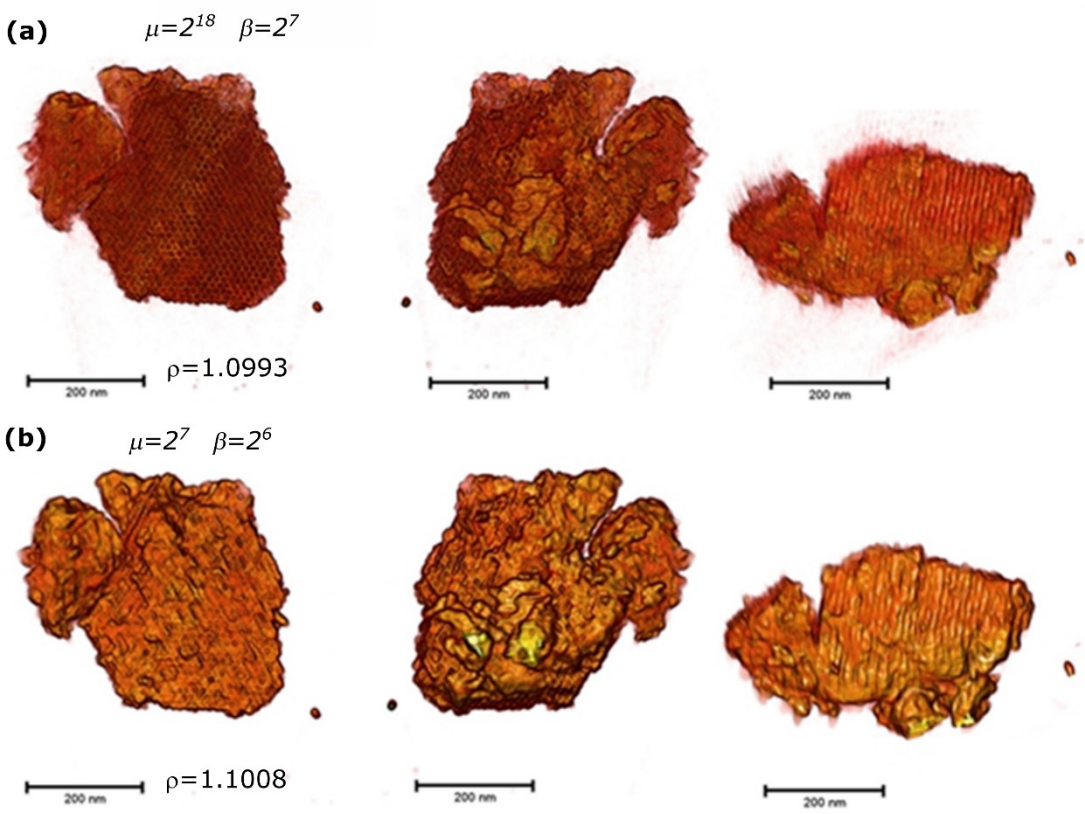

Figure 2.- Perspective views of the 3D rendered volumes reconstructed by CS-TVM3D using the automated parameter selection method (a) and using parameter values in the usual range (b). ρ is include to show the quality of the reconstructions.

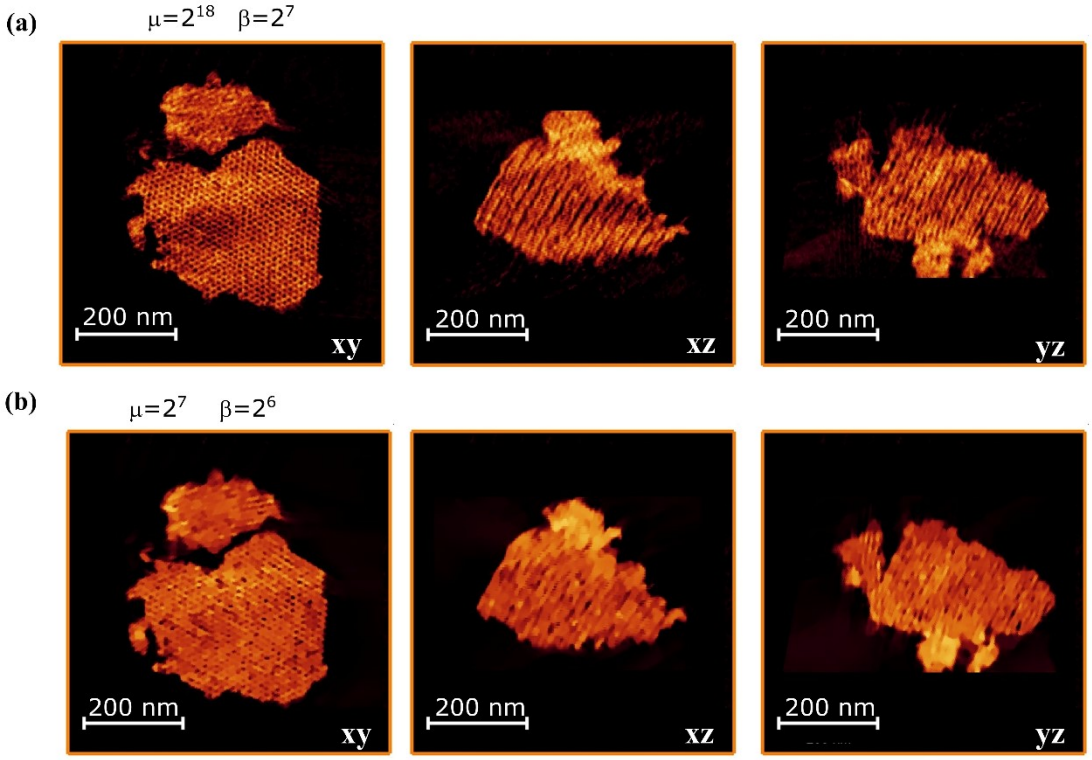

Figure 3.- Orthoslices along different directions through the 3D rendered volumes reconstructed by CS-TVM3D using the automated parameter selection method (a) and the default recommended values (b). The orthoslices in the left column were taken along a direction perpendicular to the pores, whereas those in the centre and left columns correspond to two different cuts along the pore length.

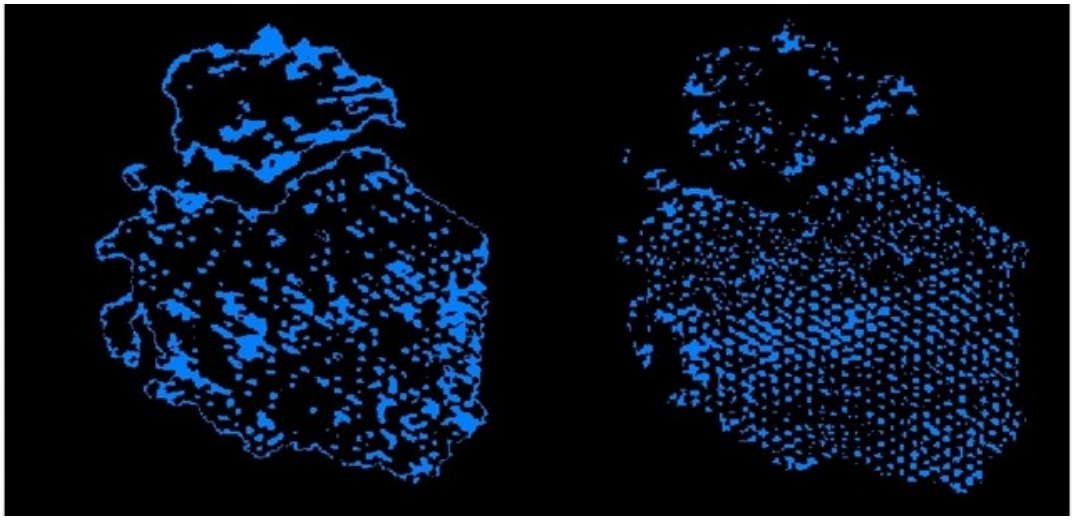

Figure 4.- Segmentation of the orthoslices shown in Figure 5 (left column). The blue areas correspond to the pores: (left) from the default recommended values; (right) from the reconstructions obtained by parameter selection.

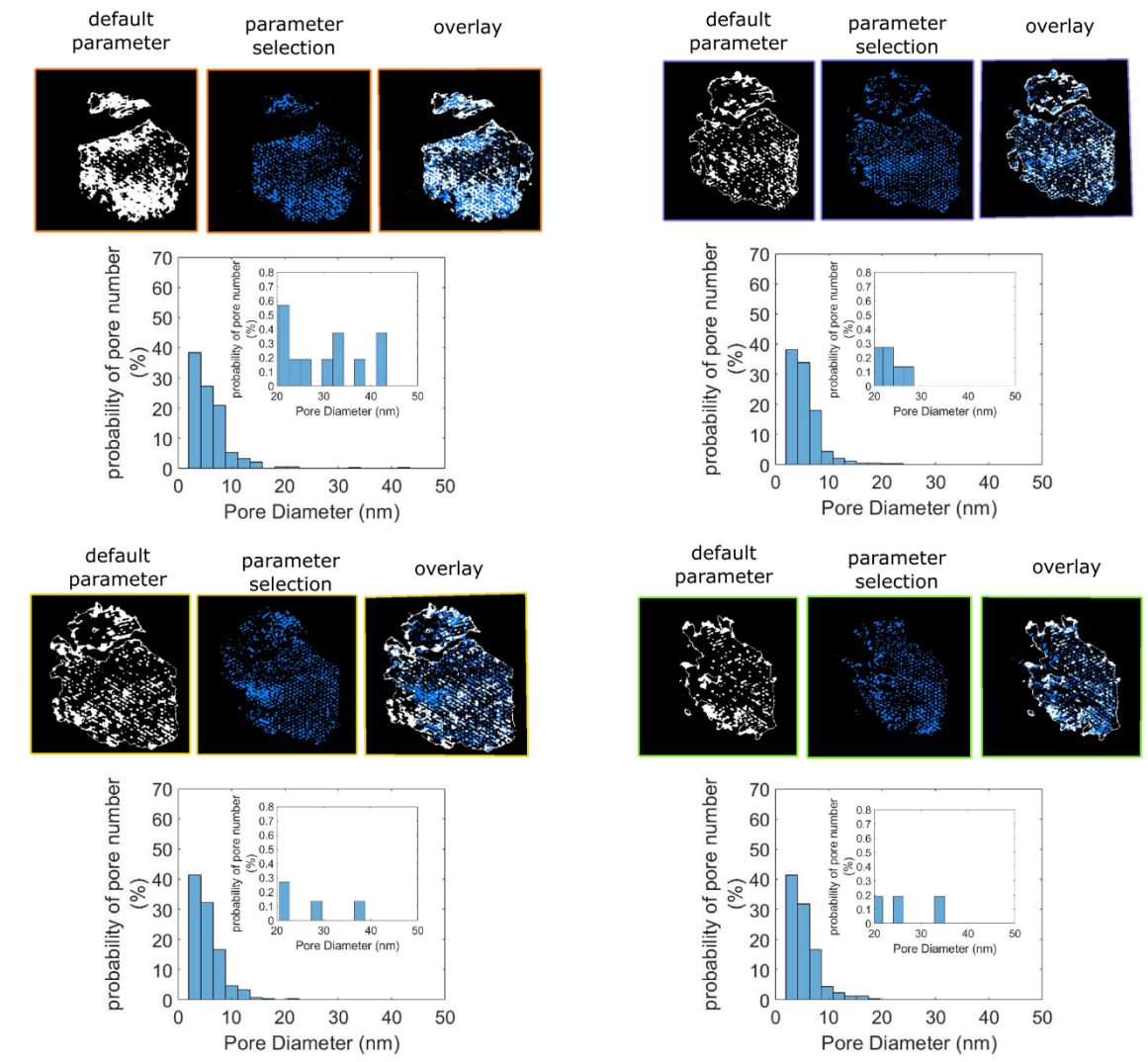

Figure 5.- Segmentations of different orthoslices through the nanoparticle are shown for the reconstructions obtained using the default recommended values and the parameter selection approaches; pore size histograms obtained from the parameter selection segmentations.

Note that, as expected, the number of objects (pores) detected in the reconstruction with the default recommended values is much smaller. Moreover, quite frequently, neighboring pores merge into larger areas, which leads to a significant contribution of pores of apparent large

diameter. On the contrary, the pore size distribution obtained after segmenting the orthoslices of the volume reconstructed by parameter selection is much narrower, showing only little contribution of very small or very large pores.

Additional orthoslices, at different positions within the volume reconstructed by the new methodology, are shown in **Figure 5 and S10** in the Supporting Information, together with their segmentations and histograms of pore size distribution. The segmentations of the orthoslices reconstructed with the default recommended values are also shown for comparison. Note how, in all cases, a rather uniform pore structure is clearly resolved in the orthoslices corresponding to the reconstruction obtained by parameter selection. Moreover, the pore width distributions estimated from each of the segmented orthoslices are quite similar to each other, covering the 0 – 20 nm width range. Considering all the pore diameter measurements in the different orthoslices, a pore size distribution with average at 6 nm was obtained, **Figure S11**, which very closely resembles that measured from N_2-physisorption (7 nm).[6a] This small underestimation, in good agreement with the results of the study performed on the nanopore phantom commented above, is related to the influence of noise in the experimental tilt series, which can only be partially avoided by the UWT denoising step.

Considering a density for amorphous carbon of 1.8 $g \cdot cm^{-3}$,[6a] a specific pore volume of 0.046 $cm^3 \cdot g^{-1}$ could also be estimated for the material, which is very similar to the micropore volume determined by physisorption, 0.053 $cm^3 \cdot g^{-1}$. Therefore, a reasonably good agreement is found between structural parameters established by the ET reconstructions performed using the new methodology and macroscopic measurements.

Similarly, segmentations of orthoslices corresponding to cuts along the pore growth direction, **Figure S12**, show a large improvement in the reconstruction along the entire length of the pores when the correct (μ,β) parameters are used.

3. Conclusion

An automated parameter selection method has been developed to optimize tomographic reconstructions using CS-TVM algorithms. This method allows the reconstruction to be obtained which closest fits the experimental tilt series within a large area of the parameter space characteristic of this algorithm, so providing the necessary certainty of having arrived at the best structural analysis possible using this type of algorithm.

The method, applied to UWT-denoised tilt series, has been tested in the 3D morphological analysis of an ordered mesoporous carbon structure and compared with the routine use of CS-TVM. While the latter failed to clearly distinguish the actual porous nature of the investigated sample, the use of the new methodology revealed the presence of an ordered, honeycomb-type arrangement of, roughly 6 nm wide, pores. Moreover, a good agreement was found between nanoscopic 3D and macroscopic measurements, which confirms the reliability of the methodology developed in this study.

Finally, it has been proved that the CS-TVM approach seems to be well suited to analyze mesoporous structures, which comprise a large family of materials with applications in catalysis, when an appropriate choice is made of the key parameters influencing this particular algorithm. Although the correct parameter combination could of course have been reached by chance, in just one trial, a systematic search adapts much better to the large variety of experimental conditions in which the tilt series can be recorded and, most importantly, removes any doubt of really having met the best possible analysis using the CS-TVM scheme.

4. Experimental Section

The synthesis of the ordered mesoporous carbon sample has been previously described elsewhere.[6a] Essentially, a two-phase method was used starting from resorcinol, formaldehyde, Pluronic F127, NH_4OH and oxalic acid as reagents in the following ratios 1: 1.39: 0.00635:

0.01: 0.125. A starting precursor solution of resorcinol and formaldehyde was prepared by mixing, for 1 h at 35 ºC, 2.20 g of resorcinol with 2.26 g of 37 wt % formaldehyde aqueous solution. Then, 2 ml of 0.1M NH_4OH was added and the resulting solution further stirred for 1 h. The resulting solution was then cooled to 18 °C for 10 minutes and further mixed, for 20 min, with a solution containing 1.60 g of F127, 8 g of water and 10 g of ethanol. Afterwards, 0.225g of oxalic acid was added to the mixture with continuous stirring. After 5-10 minutes, the clear solution became cloudy indicating phase separation. After constant stirring for a further 1 h period, the mixture was left standing overnight to obtain the polymer gel phase. This polymer gel was dried for at least 12 h at room temperature and cured at 80 ºC for 24 h. The resultant material was finally calcined at 400 °C for 3 h with a heating rate of 1ºC min^{-1} under N_2 atmosphere (100 cm^3 min^{-1}).

Gas physisorption analysis was conducted at 77K on a Micrometrics TriStar II 3020 equipment using liquid N_2. Samples were degassed at 120 ºC under vacuum for at least 12 h prior to analysis. Micrometrics software was used to calculate the Barrett, Joyner and Halenda (BJH) pore size distribution from the adsorption branches of the isotherms.

The Electron Microscopy samples were prepared by dry deposition of the catalyst powder onto a holey-carbon coated Cu grid to avoid the use of any solvent. Electron tomography experiments were performed in a FEI Titan^3 Themis 60-300 double aberration corrected microscope operated at 200 kV. A convergence angle of 9 mrad was selected in order to improve the depth of focus and a camera length of 115 mm was used. The tomography tilt serie was acquired automatically (focusing, tracking and tilting) using the software FEI Explore3D v.4.1.2. In particular, the sample was tilting from −70° to +70°, acquiring images every 2.5°. A size of 1024 x 1024 pixels was selected and dwell time of 6 us was used, providing an overall exposure time of 7s for each projection.

To denoise the tilt series, home-made scripts in MATLAB were made using WAVELAB850toolbox(http://statweb.stanford.edu/~wavelab/Wavelab_850/index_wavelab8

50.html) and the invansc package, as downloaded from http://www.cs.tut.fi/~foi/invansc/. The whole set of HAADF- STEM denoised images were aligned combining cross-correlation methods, using FEI Inspect3D v 4.0 and the landmark-based alignment implemented in TomoJ.[15] The tilt series images were resized to 512x512 px size, also background subtracted and normalized.

For the optimization of the CS-TVM parameters, the denoised, filtered and background subtracted images were reconstructed using TVM. In particular, the implementation of the TVAL3 routine using the ASTRA tomography toolbox[16] (http://www.astra-toolbox.com/index.html) was employed. Once the reconstruction parameters were optimized, the final reconstruction of the tilt series was carried out using the TVM-3D algorithm as implemented in Matlab. All the calculations were performed on an Intel Core I7 8700 workstation, 64 Gb RAM, VGA NVIDIA RTX 2070. Computation times for the individual 512×512 CS-TVM reconstruction were on the order of 8000 seconds, whereas those for the new methodology and the final TVM3D were roughly 36800 seconds. It is clear that applying our algorithm to look for a good parameter combination could require a long computational time. However, we ensure that we have obtained the best quality reconstruction within the parameter range explored thanks to this algorithm. The segmentation step was carried out using a home-developed procedure.[12] For visualization and further nanometrological analysis of the reconstructed volumes, the FEI Avizo 7.0 Fire Software was used.

Supporting Information

Supporting Information is available from the Wiley Online Library or from the author.

Acknowledgements

This work has received financial support from FEDER/MINECO (MAT2017-87579-R, MAT2016-81118-P and MTM2016-74983-C2-2-R). Junta de Andalucía is also acknowledged (MULTITOM Project, FQM334, FQM355). JMM acknowledges the Youth Employment Program (Plan de Empleo Juvenil) of Junta de Andalucía. Electron Microscopy data were acquired using the equipment at the DME-UCA node of the ELECMI Spanish Unique

Infrastructure for Electron Microscopy of Materials. We thank the University of St Andrews for a PhD scholarship for FS.

Received: ((will be filled in by the editorial staff))
Revised: ((will be filled in by the editorial staff))
Published online: ((will be filled in by the editorial staff))

References

[1] a)G. Van Tendeloo, S. Bals, S. Van Aert, J. Verbeeck, D. Van Dyck, *Adv. Mater.* **2012**, *24*, 5655-5675; b)Z. Saghi, P. A. Midgley, *Annu. Rev. Mater. Sci.* **2012**, *42*, 59-79.

[2] P. Ercius, O. Alaidi, M. J. Rames, G. Ren, *Adv. Mater.* **2015**, *27*, 5638-5663.

[3] S. M. Collins, P. A. Midgley, *Ultramicroscopy* **2017**, *180*, 133-141.

[4] a)H. Vanrompay, A. Beche, J. Verbeeck, S. Bals, *Part. Part. Syst. Char.* **2019**, *36*; b)R. Tovey, M. Benning, C. Brune, M. J. Lagerwerf, S. M. Collins, R. K. Leary, P. A. Midgley, C.-B. Schonlieb, *Inverse Problems* **2019**, *35*; c)P. Trampert, W. Wang, D. Chen, R. B. G. Ravelli, T. Dahmen, P. J. Peters, C. Kuebel, P. Slusallek, *Ultramicroscopy* **2018**, *191*, 1-10; d)K. Sentosun, I. Lobato, E. Bladt, Y. Zhang, W. J. Palenstijn, K. J. Batenburg, D. Van Dyck, S. Bals, *Part. Part. Syst. Char.* **2017**, *34*; e)Z. Saghi, M. Benning, R. Leary, M. Macias-Montero, A. Borras, P. A. Midgley, *Advanced Structural and Chemical Imaging* **2015**, *1*.

[5] a)R. Leary, Z. Saghi, P. A. Midgley, D. J. Holland, *Ultramicroscopy* **2013**, *131*, 70-91; b)B. Goris, W. Van den Broek, K. J. Batenburg, H. Heidari Mezerji, S. Bals, *Ultramicroscopy* **2012**, *113*, 120-130.

[6] a)F. Sakina, J. Manuel Munoz-Ocana, A. Bouziane, M. Lopez-Haro, R. T. Baker, *Nanoscale Adv.* **2019**, *1*, 4772-4782; b)F. J. R. Mejias, S. Trasobares, M. Lopez-Haro, R. M. Varela, J. M. G. Molinillo, J. J. Calvino, F. A. Macias, *ACS Applied Materials & Interfaces* **2019**, *11*, 41925-41934; c)R. Jurado, J. Adamcik, M. Lopez-Haro, J. A. Gonzalez-Vera, A. Ruiz-Arias, A. Sanchez-Ferrer, R. Cuesta, J. M. Dominguez-Vera, J. J. Calvino, A. Orte, R. Mezzenga, N. Galvez, *J. Am. Chem. Soc.* **2019**, *141*, 1606-1613; d)A. Gonzalez, V. Garces, L. Sabio, F. Velando, M. Lopez-Haro, N. Galvez, J. J. Calvino, J. M. Dominguez-Vera, *J. Appl. Phys.* **2019**, *126*; e)M. Dalmases, P. Torruella, J. Blanco-Portals, A. Vidal, M. Lopez-Haro, J. J. Calvino, S. Estrade, F. Peiro, A. Figuerola, *Chem. Mater.* **2018**, *30*, 6893-6902; f)M. Lopez-Haro, L. Guétaz, T. Printemps, A. Morin, S. Escribano, P. H. Jouneau, P. Bayle-Guillemaud, F. Chandezon, G. Gebel, *Nat. Commun.* **2014**, *5*, 5229; g)G. Haberfehlner, A. Orthacker, M. Albu, J.

Li, G. Kothleitner, *Nanoscale* **2014**, *6*, 14563-14569; h)Z. Saghi, D. J. Holland, R. Leary, A. Falqui, G. Bertoni, A. J. Sederman, L. F. Gladden, P. A. Midgley, *Nano Lett.* **2011**, *11*, 4666-4673.

[7] A. Chambolle, *Journal of Mathematical Imaging and Vision* **2004**, *20*, 89-97.

[8] C. Li, W. Yin, H. Jiang, Y. Zhang, *Comput. Optim. Appl.* **2013**, *56*, 507-530.

[9] F. Sakina, R. T. Baker, *Microporous Mesoporous Mater.* **2019**, *289*.

[10] a)J. Zecevic, K. P. de Jong, P. E. de Jongh, *Curr. Opin. Solid State Mater. Sci.* **2013**, *17*, 115-125; b)J. M. Thomas, R. Leary, P. A. Midgley, D. J. Holland, *J. Colloid Interface Sci.* **2013**, *392*, 7-14.

[11] a)W. Wang, A. Svidrytski, D. Wang, A. Villa, H. Hahn, U. Tallarek, C. Kuebel, *Microsc. Microanal.* **2019**, *25*, 891-902; b)S.-J. Reich, A. Svidrytski, A. Hoeltzel, J. Florek, F. Kleitz, W. Wang, C. Kuebel, D. Hlushkou, U. Tallarek, *J. Phys. Chem. C* **2018**, *122*, 12350-12361; c)G. Prieto, J. Zecevic, H. Friedrich, K. P. De Jongh, P. E. De Jongh, *Nat. Mater.* **2013**, *12*.

[12] M. Lopez-Haro, M. Tinoco, S. Fernandez-Garcia, X. Chen, A. Belen Hungria, M. Angel Cauqui, J. Juan Calvino, *Part. Part. Syst. Char.* **2018**, *35*.

[13] T. Printemps, G. Mula, D. Sette, P. Bleuet, V. Delaye, N. Bernier, A. Grenier, G. Audoit, N. Gambacorti, L. Hervé, *Ultramicroscopy* **2016**, *160*, 23-34.

[14] D. Chen, B. Goris, F. Bleichrodt, H. H. Mezerji, S. Bals, K. J. Batenburg, G. de With, H. Friedrich, *Ultramicroscopy* **2014**, *147*, 137-148.

[15] C. MessaoudiI, T. Boudier, C. O. S. Sorzano, S. Marco, *BMC Bioinformatics* **2007**, *8*, 288.

[16] W. van Aarle, W. J. Palenstijn, J. De Beenhouwer, T. Altantzis, S. Bals, K. J. Batenburg, J. Sijbers, *Ultramicroscopy* **2015**, *157*, 35-47.